Azimuthal anisotropy: Transition from hydrodynamic flow to jet suppression

Roy A. Lacey,[1,2,*] A. Taranenko,[1] R. Wei,[1] N. N. Ajitanand,[1] J. M. Alexander,[1] J. Jia,[1,2] R. Pak,[2] Dirk H. Rischke,[3,4] D. Teaney,[5,2] and K. Dusling[2]

[1]*Department of Chemistry, Stony Brook University, Stony Brook, New York 11794-3400, USA*
[2]*Physics Department, Bookhaven National Laboratory, Upton, New York 11973-5000, USA*
[3]*Frankfurt Institute for Advanced Studies (FIAS), D-60438 Frankfurt am Main, Germany*
[4]*Institut für Theoretische Physik, Johann Wolfgang Goethe-Universität, D-60438 Frankfurt am Main, Germany*
[5]*Department of Physics, Stony Brook University, Stony Brook, New York 11794-3800, USA*

(Received 26 May 2010; published 30 September 2010)

Measured second and fourth azimuthal anisotropy coefficients $v_{2,4}(N_{\rm part}, p_T)$ are scaled with the initial eccentricity $\varepsilon_{2,4}(N_{\rm part})$ of the collision zone and studied as a function of the number of participants $N_{\rm part}$ and the transverse momenta p_T. Scaling violations are observed for $p_T \lesssim 3$ GeV/c, consistent with a p_T^2 dependence of viscous corrections and a linear increase of the relaxation time with p_T. These empirical viscous corrections to flow and the thermal distribution function at freeze-out constrain estimates of the specific viscosity and the freeze-out temperature for two different models for the initial collision geometry. The apparent viscous corrections exhibit a sharp maximum for $p_T \gtrsim 3$ GeV/c, suggesting a breakdown of the hydrodynamic ansatz and the onset of a change from flow-driven to suppression-driven anisotropy.

DOI: 10.1103/PhysRevC.82.034910 PACS number(s): 25.75.Ld, 25.75.Dw, 25.75.Nq

A central objective of the experimental program at the Relativistic Heavy Ion Collider (RHIC) is to delineate the thermodynamic and transport properties of the hot and dense matter produced in energetic heavy-ion collisions. This matter can equilibrate to form a hot plasma of quarks and gluons (QGP) [1], which rapidly expands, cools, and then hadronizes to produce the observed particles. The hydrodynamic-like expansion of the QGP, as well as its interactions with hard scattered partons, results in the anisotropic emission of hadrons relative to the reaction plane. At midrapidity, the magnitude of this momentum anisotropy is characterized by the even-order Fourier coefficients, $v_n = \langle e^{in(\Delta\phi)} \rangle$, $n = 2, 4, \ldots$, where $\Delta\phi$ is the azimuth of an emitted hadron about the reaction plane and brackets denote averaging over particles and events.

The coefficients for hadrons with low transverse momenta ($p_T \lesssim 2$ GeV/c) can be understood in terms of *flow* or partonic interactions, which drive pressure gradients in an initial "almond-shaped" collision zone produced in noncentral collisions [2–5]. For higher transverse momenta ($p_T \gtrsim 5$ GeV/c), the coefficients can be attributed to jet quenching [6]—the process by which hard scattered partons interact and lose energy in the hot and dense QGP prior to fragmenting into hadrons. This energy loss manifests as a suppression of hadron yields [7], which depends on the average distance that partons propagate through the QGP. Thus, $v_{2,4}$ stem from the fact that partons that traverse the QGP medium in a direction parallel (perpendicular) to the reaction plane result in less (more) suppression due to shorter (longer) parton propagation lengths [8–10]. This path-length dependence is exemplified in the recently observed scaling patterns for hadron suppression [11,12]. The transition from flow-driven to suppression-driven anisotropy is still poorly understood, and it remains a challenge to find a single consistent theoretical framework that gives an explanation of $v_{2,4}$ measurements over the full p_T range.

The magnitude of $v_{2,4}$ as well as their detailed dependence on p_T and collision centrality (or number of participants $N_{\rm part}$) give invaluable insights on the thermodynamic and transport coefficients of the QGP. In particular, flow measurements [$v_2(p_T)$ and $v_2(N_{\rm part})$] have been used to estimate the specific shear viscosity (i.e., the ratio of shear viscosity η to entropy density s of the plasma) via comparisons to viscous relativistic hydrodynamic calculations [13–17]. The reliability of these $\frac{\eta}{s}$ estimates is influenced not only by the uncertainties in the initial conditions for hydrodynamic evolution but also by ambiguities in the departure from equilibrium on the freeze-out surface. For a viscous fluid, this distribution (f) is of the form

$$\frac{dN}{dy p_T dp_T d\phi} \sim f_0 + \delta f \equiv f_0\left(1 + C\left(\frac{p_T}{T_f}\right)^{2-\alpha}\right), \qquad (1)$$

where f_0 is the equilibrium distribution, T_f is the freeze-out temperature, $C \approx \eta/(3\tau s T_f)$, and α ranges between 0 and 1 [18,19]; τ is the time scale of the expansion. The factor δf, which results from a finite shear viscosity, is known to dominate the calculated viscous corrections to $v_2(p_T)$ for $p_T \gtrsim 1$ GeV/c [19]. However, its momentum dependence and associated relaxation time $\tau_R(p)$ is not known *a priori*, and it is unclear whether it is proportional to p_T^2 ($\alpha = 0$ and $\tau_R \propto p$) as has been generally assumed in hydrodynamic calculations [13–17,19]. The freeze-out temperature and the p_T for which large viscous corrections render a breakdown of viscous hydrodynamics are also not well established experimentally.

The influence of viscous corrections on the eccentricity-scaled anisotropy coefficient $\frac{v_2(N_{\rm part}, p_T)}{\varepsilon_2(N_{\rm part})}$ is illustrated in Figs. 1(a) and 1(b) where the results of hydrodynamic simulations (with the code of Dusling and Teaney [19]) are shown for $\frac{\eta}{s} = 0$ and 0.2, respectively. Figure 1(b) shows that viscous effects reduce $v_2(N_{\rm part}, p_T)$ and break the scale

*Roy.Lacey@Stonybrook.edu

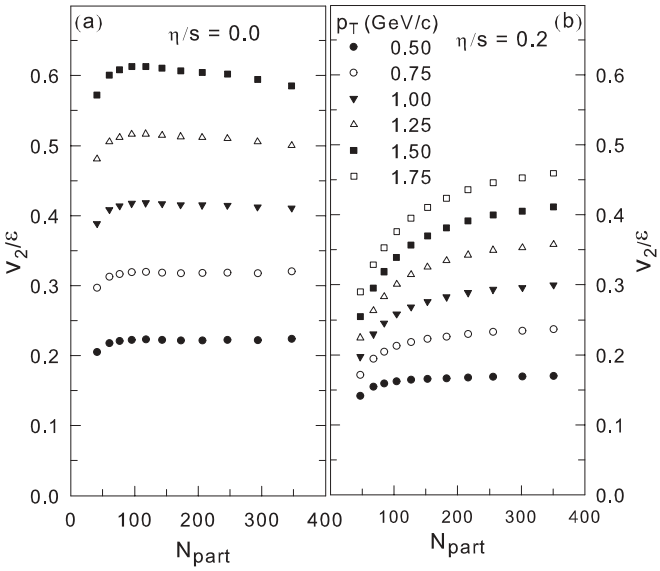

FIG. 1. Comparison of v_2/ε_2 vs $N_{\rm part}$ for several p_T selections, obtained from perfect fluid (a) and viscous hydrodynamic (b) simulations [19] of Au + Au collisions.

invariance of ideal hydrodynamics evidenced in Fig. 1(a); that is, there are deviations away from the essentially flat $N_{\rm part}$ dependence expected for ideal hydrodynamic scaling. These deviations from eccentricity scaling can be used to estimate and characterize viscous corrections [19–23].

Here, we use the eccentricity-scaled anisotropy coefficients,

$$\frac{v_2(N_{\rm part}, p_T)}{\varepsilon_2(N_{\rm part})}$$

and

$$\frac{v_4(N_{\rm part}, p_T)}{\varepsilon_4(N_{\rm part})},$$

to extract estimates of the viscous corrections to $v_{2,4}(p_T, N_{\rm part})$. In turn, we use these estimates to explore the p_T dependence of δf and the transition from flow-driven to suppression-driven anisotropy. We find viscous correction factors for $p_T \lesssim 3$ GeV/c that validate the commonly assumed p_T^2 dependence of δf, and give constrained estimates for $\frac{\eta}{s}$ and the freeze-out temperature T_f. For $p_T \gtrsim 3$ GeV/c, the apparent viscous corrections signal a breakdown of the hydrodynamic ansatz.

The $v_{2,4}$ data employed in our analysis are selected from the high-precision PHENIX measurements recently reported for Au + Au collisions at $\sqrt{s_{NN}} = 200$ GeV [24]. These data show that both v_2 and v_4 have a strong dependence on p_T and centrality. The large increase in $v_{2,4}(p_T)$ from central to peripheral events is especially important to our study of viscous corrections.

Monte Carlo (MC) simulations [25] were used to calculate the event-averaged geometric quantities used in our analysis. For each collision, the values for $N_{\rm part}$ and the number of binary collisions $N_{\rm coll}$ were determined via the Glauber ansatz [26]. The associated values for the transverse size $\bar{R}$, area S, and eccentricities $\varepsilon_{2,4}$ were then evaluated from the two-dimensional density of sources in the transverse plane $\rho_s(\mathbf{r}_\perp)$ using two principal models: a modified version of the MC-Glauber approach [26] and the factorized Kharzeev-Levin-Nardi (MC-KLN) model [27,28].

For each event, we compute an event-shape vector S_n and the azimuth of rotation Ψ_n^* for the nth harmonic of the shape profile [25]:

$$S_{nx} \equiv S_n \cos(n\Psi_n^*) = \int d\mathbf{r}_\perp \rho_s(\mathbf{r}_\perp)\omega(\mathbf{r}_\perp)\cos(n\phi),$$

$$S_{ny} \equiv S_n \sin(n\Psi_n^*) = \int d\mathbf{r}_\perp \rho_s(\mathbf{r}_\perp)\omega(\mathbf{r}_\perp)\sin(n\phi),$$

$$\Psi_n^* = \frac{1}{n}\tan^{-1}\left(\frac{S_{ny}}{S_{nx}}\right),$$

where ϕ is the azimuthal angle of each source and the weight $\omega(\mathbf{r}_\perp) = {\mathbf{r}_\perp}^2$; $\varepsilon_{2,4}$ were calculated as

$$\varepsilon_2 = \langle\cos 2(\phi - \Psi_2^*)\rangle, \quad \varepsilon_4 = \langle\cos 4(\phi - \Psi_2^*)\rangle, \qquad (2)$$

where the brackets denote averaging over sources, as well as events belonging to a particular centrality or impact parameter range. For the MC-Glauber calculations, an additional entropy-density weight was applied reflecting the combination of spatial coordinates of participating nucleons and binary collisions [29]:

$$\rho_s(\mathbf{r}_\perp) \propto \left[\frac{(1-\alpha_1)}{2}\frac{dN_{\rm part}}{d^2\mathbf{r}_\perp} + \alpha_1 \frac{dN_{\rm coll}}{d^2\mathbf{r}_\perp}\right],$$

where $\alpha_1 = 0.14$ was constrained by multiplicity measurements as a function of $N_{\rm part}$ for Au + Au collisions [30]. Note that $\varepsilon_{2,4}$ [cf. Eq. (2)] correspond to $v_{2,4}$ measurements in the so-called participant plane [31]; this is analogous to the measurement of $v_{2,4}$ with respect to the second-order event plane as described in Ref. [24]. A correlation between the principal axes of the quadrupole (Ψ_2^*) and hexadecapole (Ψ_4^*) density profiles was also introduced to account for contributions to v_4 from v_2 [25]. This correlation has a significant influence only on ε_4 in the most central collisions [25].

Figures 2 and 3 show eccentricity-scaled values of $v_{2,4}(p_T, N_{\rm part})$ obtained with MC-KLN eccentricities for several p_T cuts. The low-p_T selections are almost flat, that is, small scaling violations. These violations gradually increase with p_T over the p_T range indicated in Fig. 2. That is, the data points slope upward progressively (from low to high $N_{\rm part}$) as the $\langle p_T\rangle$ is increased. Figure 3 shows that this trend reverses to give scaling violations that decrease with increasing $\langle p_T\rangle$, for $\langle p_T\rangle \gtrsim 3$ GeV/c. This inversion could be an indication for the onset of suppression-driven anisotropy as discussed in what follows. Similar scaling performed with MC-Glauber eccentricities shows the same trends exhibited in Figs. 2 and 3, albeit with larger scaling violations.

In lieu of detailed model comparisons [32], we estimate the magnitude of the viscous corrections by parametrizing the observed scaling violations with a Knudsen number ($K = \lambda/\bar{R}$) ansatz akin to that in Refs. [20,21];

$$\frac{v_{2k}(p_T)}{\varepsilon_{2k}} = \frac{v_{2k}^h(p_T)}{\varepsilon_{2k}}\left\{\frac{1}{1 + [K^*(p_T)/K_0]}\right\}^k \quad k = 1, 2, \ldots, \qquad (3)$$

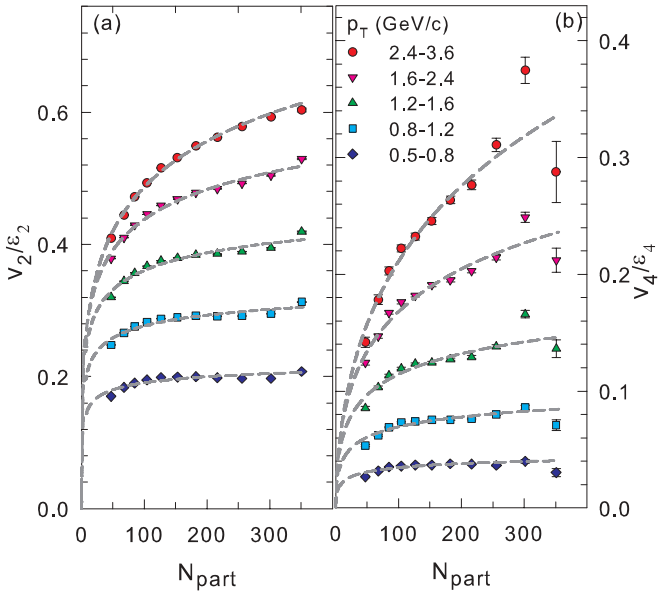

FIG. 2. (Color online) Comparison of v_2/ε_2 vs $N_{\rm part}$ (a) and v_4/ε_4 vs $N_{\rm part}$ (b) for several p_T selections as indicated [24]. The dashed curves indicate a simultaneous fit to the data in (a) and (b) (for each p_T) with Eq. (3). The $v_{2,4}$ data are from Ref. [24].

where $K^*(p_T)$ characterizes the magnitude of the viscous correction for a given p_T, $[v_{2,4}^h(p_T)]/\varepsilon_{2,4}$ are the eccentricity-scaled coefficients expected from ideal hydrodynamics, λ is the mean-free path, and K_0 is a constant estimated to be 0.7 ± 0.03 with the aid of a transport model [33].

For each p_T selection, $[K^*(p_T)]^{-1} = \beta(p_T)\frac{1}{S}\frac{dN}{dy}$; ($\frac{dN}{dy} \propto N_{\rm part}$) is evaluated by fitting

$$\frac{v_{2,4}(p_T, N_{\rm part})}{\varepsilon_{2,4}(N_{\rm part})}$$

verus $N_{\rm part}$ with Eq. (3) (cf. curves in Figs. 2 and 3). The fit parameters $\beta(p_T)$, so obtained, allow the determination of $K^*(p_T)$ as a function of $N_{\rm part}$. Note that a model uncertainty

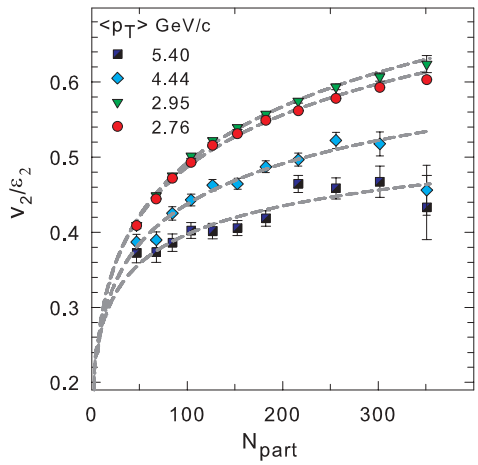

FIG. 3. (Color online) v_2/ε_2 vs $N_{\rm part}$ for several $\langle p_T\rangle$ values as indicated. The filled circles are the same as in Fig. 2(a). The dashed curves show fits to the data obtained with Eq. (3). The v_2 data are from Ref. [24].

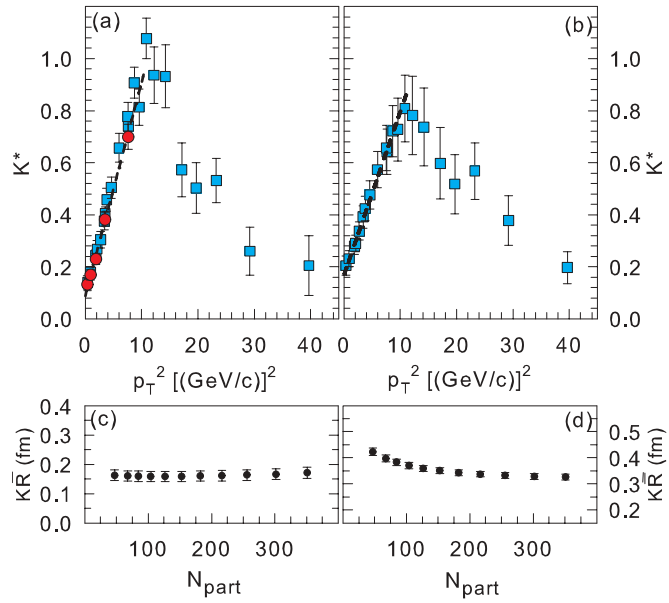

FIG. 4. (Color online) K^* vs $\langle p_T\rangle^2$ (a) and (b), and $K\bar{R}$ vs $N_{\rm part}$ (c) and (d), extracted with MC-KLN (left panels) and MC-Glauber geometry (right panels). The filled circles in (a) indicate results from the simultaneous fits shown in Fig. 2. The dashed curves in (a) and (b) show a fit to the data for $\langle p_T\rangle^2 \lesssim 10$ [GeV/c]^2.

in the value of K_0 would lead to an accompanying uncertainty in the magnitude of K^*. However, the consistency of our procedure with hydrodynamic models has been tested via fits to $\frac{v_2(N_{\rm part}, p_T)}{\epsilon_2(N_{\rm part})}$ versus $N_{\rm part}$, obtained for specified values of $\frac{\eta}{s}$ [23]. These fits lead to $\frac{\eta}{s}$ values that reproduce the input values to the hydrodynamic simulations.

Figures 4(a) and 4(b) show the values of K^* versus p_T^2, extracted for $N_{\rm part} \sim 351$ with MC-KLN and MC-Glauber geometries respectively (the plots for other values of $N_{\rm part}$ show similar trends but with different intercepts). The filled circles in Fig. 4(a) show results from the simultaneous fits indicated by the dashed curves in Figs. 2(a) and 2(b). The squares show results for fits that employ only

$$\frac{v_2(p_T, N_{\rm part})}{\varepsilon_2(N_{\rm part})}$$

data [24]; both are in good agreement.

The K^* values shown in Figs. 4(a) and 4(b) indicate a linear dependence on p_T^2, for $\langle p_T\rangle^2 \lesssim 10$ [GeV/c]^2, that demonstrates a nonzero viscosity and the p_T^2 dependence of δf commonly assumed in hydrodynamic simulations [13–17,19]. In contrast, the data for $10 \lesssim \langle p_T\rangle^2 \lesssim 40$ [GeV/c]^2 show a striking trend inversion. We interpret this as a signal for the breakdown of the hydrodynamic ansatz when $K^* \sim 1$, as well as an indication for the onset of suppression-driven anisotropy. Note that such a scenario would lead to improved eccentricity scaling for $p_T \gtrsim 3$ GeV/c because the eccentricity encodes the variation of the path length relative to the orientation of the reaction plane, and the suppression of hadron yields has been found to increase as $\frac{1}{\sqrt{p_T}}$ for a similar p_T range [12].

To obtain estimates for K and T_f for each value of $N_{\rm part}$, we use our observation that $K^*(p_T) \propto p_T^2$ in conjunction with

the first-order expansion of

$$v_2(p_T) = \langle \cos(2\Delta\phi) \rangle_{p_T} \equiv \frac{\int_{-\pi}^{\pi} d\Delta\phi \, \cos(2\Delta\phi)[\,(d^3N)/(dy\, p_t\, dp_t\, d\Delta\phi)]}{\int_{-\pi}^{\pi} d\Delta\phi \, [(d^3N)/(dy\, p_t\, dp_t\, d\Delta\phi)]},$$

to obtain the expression $K^*(p_T) = K + \frac{B}{T_f}\left(\frac{p_T}{T_f}\right)^2$; the constant B was cross-checked via fits to the results from hydrodynamic simulations. Fits to K^* versus p_T^2 were performed with this fit function. The dashed curve in Fig. 4(a) indicates such a fit for $\langle p_T \rangle^2 \lesssim 10\,[\mathrm{GeV/c}]^2$; it gives the values $K = 0.09 \pm 0.01$ (from the intercept) and $T_f = 162 \pm 11$ MeV (from the slope). The same fit to the K^* values in Fig. 4(b) (extracted with MC-Glauber eccentricities) gives the values $K = 0.17 \pm 0.007$ and $T_f = 173 \pm 11$ MeV. These same values of T_f are indicated by the fits to the data for other N_{part} values, for both data sets. However, as to be expected, the extracted K values vary with N_{part}. Note again that a model uncertainty in the value of K_0 would lead to an accompanying uncertainty in the magnitude of K and the associated values for λ and $\frac{\eta}{s}$ discussed in what follows. The estimates for T_f are similar to the chemical freeze-out temperature ($T_c \sim 165$ MeV) obtained for a broad range of collision energies [34].

Figures 4(c) and 4(d) show the product $K\bar{R}$ verus N_{part}, obtained with MC-KLN and MC-Glauber geometry respectively. Figure 4(c) indicates that the estimated value $\lambda \sim 0.17 \pm 0.018$ fm is essentially independent of N_{part}. Figure 4(d) indicates a larger estimate for central collisions $\lambda \sim 0.33 \pm 0.02$ fm and a mild increase as collisions become more peripheral. While our analysis seems more consistent for the MC-KLN geometry, the model dependencies apparent in Fig. 4 highlight the importance of experimental signatures that can distinguish MC-KLN and MC-Glauber collision geometries [25].

Estimates for $\frac{\eta}{s}$ were obtained via the expression $\frac{\eta}{s} \approx \lambda T c_s \equiv (\bar{R} K T c_s)$, where the sound speed $c_s = 0.47 \pm 0.03$ c was obtained from lattice calculations [35] for the mean temperature $T = 220 \pm 20$ MeV [36]. This gives the estimates $4\pi\frac{\eta}{s} = 1.1 \pm 0.1$ and $4\pi\frac{\eta}{s} = 2.1 \pm 0.2$ for the K values extracted using MC-KLN and MC-Glauber eccentricities (respectively) in central and midcentral collisions. These estimates are in agreement with the low value from prior extractions [13–17,19,21,23,37–39].

In summary, we have used eccentricity-scaled anisotropy coefficients to extract estimates of the strength and role of the viscous corrections. These estimates show a quadratic increase with p_T (for $p_T \lesssim 3$ GeV/c) that validates a nonzero viscosity and a relaxation time that grows with p_T. The extracted viscous corrections also constrain the estimates $4\pi\frac{\eta}{s} \sim 1.1 \pm 0.1$ (2.1 ± 0.2) and $T_f = 162 \pm 11$ MeV (173 ± 11 MeV) for MC-KLN (MC-Glauber) collision geometries for a strongly coupled plasma. The onset of a transition from flow-driven to suppression-driven anisotropy is signaled by a sharp maximum of the apparent viscous corrections for $p_T \gtrsim 3$ GeV/c. These results provide valuable constraints for input parameters to more detailed viscous hydrodynamic calculations.

This research is supported by the US DOE under Contract No. DE-FG02-87ER40331.A008 and by the NSF under Award No. PHY-0701487.

[1] E. V. Shuryak, Phys. Lett. B **78**, 150 (1978).
[2] J.-Y. Ollitrault, Phys. Rev. D **46**, 229 (1992).
[3] U. Heinz and P. Kolb, Nucl. Phys. A **702**, 269 (2002).
[4] E. Shuryak, Prog. Part. Nucl. Phys. **62**, 48 (2009).
[5] R. Peschanski and E. N. Saridakis, Phys. Rev. C **80**, 024907 (2009).
[6] M. Gyulassy and X.-N. Wang, Nucl. Phys. B **420**, 583 (1994).
[7] K. Adcox *et al.*, Phys. Rev. Lett. **88**, 022301 (2002).
[8] M. Gyulassy, I. Vitev, and X. N. Wang, Phys. Rev. Lett. **86**, 2537 (2001).
[9] X.-N. Wang, Phys. Rev. C **63**, 054902 (2001).
[10] J. Liao and E. Shuryak, Phys. Rev. Lett. **102**, 202302 (2009).
[11] R. A. Lacey, N. N. Ajitanand, J. M. Alexander, X. Gong, J. Jia, A. Taranenko, and R. Wei, Phys. Rev. C **80**, 051901 (2009).
[12] R. A. Lacey *et al.*, Phys. Rev. Lett. **103**, 142302 (2009).
[13] P. Romatschke and U. Romatschke, Phys. Rev. Lett. **99**, 172301 (2007).
[14] M. Luzum and P. Romatschke, Phys. Rev. C **78**, 034915 (2008).
[15] H. Song and U. W. Heinz, J. Phys. G **36**, 064033 (2009).
[16] A. K. Chaudhuri, J. Phys. G **37**, 075011 (2010).
[17] G. S. Denicol, T. Kodama, and T. Koide, arXiv:1002.2394 [nucl-th].
[18] D. Teaney, Phys. Rev. C **68**, 034913 (2003).
[19] K. Dusling, G. D. Moore, and D. Teaney, arXiv:0909.0754 [nucl-th].
[20] R. S. Bhalerao *et al.*, Phys. Lett. B **627**, 49 (2005).
[21] H.-J. Drescher, A. Dumitru, C. Gombeaud, and J.-Y. Ollitrault, Phys. Rev. C **76**, 024905 (2007).
[22] H. Song and U. W. Heinz, Phys. Rev. C **78**, 024902 (2008).
[23] R. A. Lacey, A. Taranenko, and R. Wei, arXiv:0905.4368 [nucl-ex].
[24] A. Adare *et al.*, arXiv:1003.5586 [nucl-ex].
[25] R. A. Lacey *et al.*, arXiv:1002.0649 [nucl-ex].
[26] M. L. Miller, K. Reygers, S. J. Sanders, and P. Steinberg, Annu. Rev. Nucl. Part. Sci. **57**, 205 (2007).
[27] T. Lappi and R. Venugopalan, Phys. Rev. C **74**, 054905 (2006).
[28] H.-J. Drescher and Y. Nara, Phys. Rev. C **76**, 041903 (2007).
[29] T. Hirano and Y. Nara, Phys. Rev. C **79**, 064904 (2009).
[30] B. B. Back *et al.*, Phys. Rev. C **70**, 021902 (2004).
[31] B. Alver *et al.*, Phys. Rev. Lett. **98**, 242302 (2007).
[32] Such comparisons are in progress and will be presented elsewhere.
[33] C. Gombeaud and J. Y. Ollitrault, Phys. Rev. C **77**, 054904 (2008).
[34] J. Cleymans, H. Oeschler, K. Redlich, and S. Wheaton, Phys. Rev. C **73**, 034905 (2006).
[35] P. Huovinen and P. Petreczky, Nucl. Phys. A **837**, 26 (2010).
[36] A. Adare *et al.*, Phys. Rev. Lett. **104**, 132301 (2010).
[37] R. A. Lacey *et al.*, Phys. Rev. Lett. **98**, 092301 (2007).
[38] A. Adare *et al.*, Phys. Rev. Lett. **98**, 172301 (2007).
[39] Z. Xu, C. Greiner, and H. Stocker, Phys. Rev. Lett. **101**, 082302 (2008).